Received: 17 April 2021 | Revised: 17 July 2021 | Accepted: 13 September 2021

DOI: 10.1049/rpg2.12307

IET Renewable Power Generation

The Institution of Engineering and Technology WILEY

ORIGINAL RESEARCH PAPER

Control strategy for direct voltage and frequency stability enhancement in HVAC/HVDC grids

Neda Azizi[1] | **Hassan Moradi CheshmehBeigi**[1] | **Kumars Rouzbehi**[2]

[1] Department of Electrical Engineering, Razi University, Kermanshah, Iran

[2] Department of System Engineering and Automatic Control, University of Seville, Seville, Spain

Correspondence
Hassan Moradi CheshmehBeigi, Tagh-e-Bostan, University St., Kermanshah, Iran, Postal Code: 6714414971.
Email: ha.moradi@razi.ac.ir

Abstract

Direct voltage fluctuations due to the presence of relatively large DC reactors (as an essential part of HVDC breakers), lack of inertia, and unwanted frequency fluctuations in the AC side of HVDC grids, have major consequences on the stability of HVAC/HVDC grids. The use of the DC Power System Stabilizer (DC-PSS) can damp and eliminate voltage oscillations caused by the presence of the DC reactors. However, DC-PSS cannot address the issues of inertia and unwanted frequency fluctuations. A method to improve inertia is proposed here that can operate well with the droop controller, and DC-PSS does not interfere with power-sharing and does not interact with any of these elements. Since the presence of a droop controller in HVAC/HVDC grids associates with power and direct voltage, the method proposed here can improve direct voltage fluctuations by eliminating severe power peaks. Moreover, this method does not change the voltage level of the entire system, so there is no need to change the set-points of controllers. In addition, all parameters of the controllers are tuned by an intelligent algorithm, and the Participation factor (PF) scheme is used to find the proper placement of the proposed controller.

1 | INTRODUCTION

Given the long distances between offshore wind farms and onshore power grids and the need for bulk power transmission, High Voltage Direct Current (HVDC) systems became a promising solution [1]. In this paradigm, there are issues such as frequency conversion, area synchronization, and controllability [2–4]. With the advancement and developments of HVDC systems and the introduction of Multi-Terminal HVDC (MT-HVDC) systems, control and direct voltage dynamic stability are becoming as important as AC frequency stability in traditional power systems. MT-HVDC classic control methods can be generally divided into two categories: Master-Slave Control (MSC), and droop control strategy [5]. In MSC strategy, only one power converter is dedicated to direct voltage control, and the rest of the power converters have the task of regulating the injected power to the AC grid. In [6] and [7] several coordinated control methods based on the MSC strategy have been proposed, but the common drawback of these strategies is that the power converter station is also paralyzed by tripping the power converter station. Another issue is that the MSC method is based on communications and the controller performance is affected by communication delays [8].Electromechanical features distinguish the power converters from synchronous generators. Consequently, the static and dynamic characteristics of the formed new power generation units are different from those of synchronous generators [9]. The static features change by the droop controller in [10] and energy storage in [11]. One of the disadvantages of having power converters is that they prevent the entrance of kinetic energy in the inertia of renewable energy sources into the network to reduce system transients. Therefore, with the high penetration of power converters, the frequency stability of the power system and consequently the stability of the whole system is compromised, so that the control system may not be able to have acceptable performance. One of the main factors in improving the stability of such systems is inertia improvement [12]. The methods presented in [13–15] enable the wind generating units to emulate inertia during the fault or disturbance in the AC side. In [14], a method for inertia emulation via rotor energy is presented. In [15], the inertia of the system is provided by controlling the output power of the inverter according to frequency variations. However, the problem with these methods is that it is very difficult to recover and restore the rotor speed after acceleration. In [13], a time

derivative grid frequency control strategy is used to adjust the power and inertia via the power converters, but this method has the same rotor speed recovery issue as the proposed method in [15]. The INEC inertia control algorithm in VSC-HVDC systems has been investigated to improve the stability of frequency under the disturbances of the AC side of the system in [16–18] although the problem is that in these methods the existence of large capacitors increases cost and dynamic response of the controllers [19]. Besides, this method changes the voltage levels of the entire system, thus requiring a set-point change for all the controllers. In an HVDC grid, the lack of inertia [2, 16, 17] and the introduction of large DC reactors through the installed HVDC breakers [20] can lead to unstable direct voltages and will require additional control. Besides, the stability of the system is reliant on balancing generation, demand, and power losses [20]. Also, more studies on inertia improvement have focused on the problem of inertia emulation in different ways and only a few of them have investigated its optimal placement [21]. Methods for improving stability in weak grids are classified into several categories. These categories include filter and parameters design of controller [22, 23] with a trade-off between stability and performance, stability analysis focusing on the interaction between network impedance and PLL [24, 25]. Delay and impedance phase compensators have been investigated in [26, 27], however, compensators are only effective in the steady-state condition. Also, virtual impedance was used early on to distribute active and reactive power between parallel inverters [28–30].

This paper proposes a method for inertia improvement that operates alongside the droop controller, so that, it does not disturb the load sharing in the grid. The energy to do so comes from the sub-module capacitors of the Modular Multilevel Converter (MMC)s. In this method, the frequency of the AC side is measured and it is combined with inertia. Then, damping signals from DC-PSS will be injected into the droop controller loop. Both of these signals will be compared with the measured active power to be applied to the power controller as a power reference. As mentioned, using this method of inertia emulation does not prevent droop controller operation and power-sharing and does not change the voltage level of the whole system. Therefore, there is no need to change set points for controllers. Also in this paper, the particle swarm optimization (PSO) algorithm is used to tune the parameters, and the participation factor method is used to investigate the optimal location of the proposed controller.

In summary, contributions of this research are:

- This paper proposes a method for stability improvement of the HVAC/HVDC grid by inertia emulation.
- The proposed method is applied to the droop controller so that in addition to the inertia emulation to maintain the stability of the HVAC/HVDC grid, it does not disturb the system power-sharing.
- This method does not change the voltage level of the entire system, so there is no need to change a set point for the controllers.

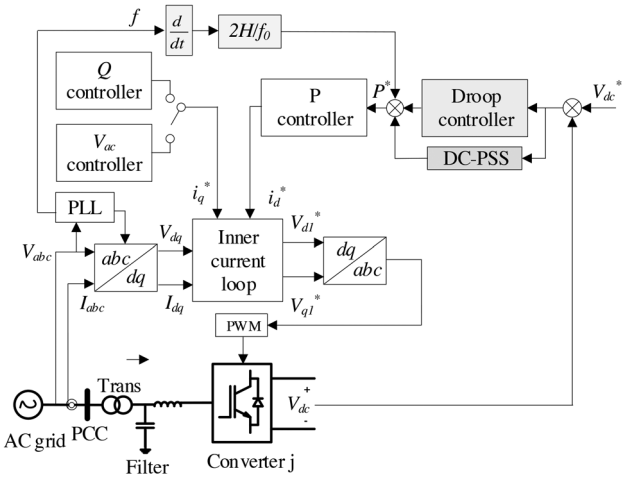

FIGURE 1 Overall control system

- The proposed method, in addition to improving the frequency stability of the AC side through the inertia emulation, also enhances the voltage stability on the DC side.
- This method provides transient damping and eliminating voltage oscillations caused by the effect of DC reactors.

The rest of the paper is divided into sections as follows: The proposed method is explained in Section 2. Section 3 is devoted to small-signal analysis. Section 4 presents the simulation results. Remarks and conclusions are presented in Section 5.

2 | PROPOSED METHOD FOR STABILITY IMPROVEMENT

Figure 1 shows an MMC station integrated into the AC grid.

The proposed method consists of the inertia emulation loop and DC-PSS.

2.1 | Inertia emulation loop

The inertia of the synchronous generators of AC systems and the energy stored in the capacitors of DC systems are analogous [12, 31]. Total stored kinetic energy (*KE*) due to the difference between the input mechanical power and the output electrical power of a synchronous generator is equal to:

$$KE = \sum_{p=1}^{N} \frac{1}{2} J_p \omega^2 \tag{1}$$

where the moment of inertia of the p-th synchronous generator is shown by J_p, and the number of generators in the power system is shown by N.

In HVDC grids, stored energy in the grid capacitors is an indicator of energy balancing.

$$CE = \sum_{p=1}^{N_c} \frac{1}{2} C_{SM,p} v_{SM,avg,p}^2 \times \left(6N_{SM,p}\right) \tag{2}$$

where capacitor energy is CE, the number of MMCs is N_c and the direct voltage of the p-th submodule capacitor of the MMC is $v_{SM,avg,p}$. As it is seen, Equation (2) is analogous to Equation (1). Unlike frequency, which is a global parameter, direct voltage is a local parameter. According to Equation (2), any changes in CE are due to the difference between the input power and the output power of the capacitors. Consequently, the capacitors of the HVDC grid, based on voltage changes, have the same function as the AC grid inertia [12].

In a synchronous generator, the inertia constant equation is shown in Equation (3), where KE is the kinetic energy stored in the rotating object and its unit is (MVA.Sec). Also, J is the inertia moment and S_M is the nominal power.

$$H = \frac{KE}{S_M} = \frac{\frac{1}{2} J\omega^2}{S_M} \tag{3}$$

The time constant of the capacitor is given by:

$$\tau = \frac{W_E}{S_{VSC}} = \frac{\frac{1}{2} CNV_{DC}^2}{S_{VSC}} \tag{4}$$

The angular motion equation of the synchronous machine is shown by:

$$\frac{2H}{f_o} \frac{df}{dt} = P_m - P_E = \Delta P_1 \ (pu) \tag{5}$$

Also, the power change of MMC can be written in the form of:

$$\frac{dW_{MMC}}{dt} = P_{in} - P_{out} = \Delta P_2 \left(pu\right) \tag{6}$$

The common structure of an MMC contains six arms. Each arm is composed of an arm reactor and several submodules (N_{SM}). The DC voltage (V_{DC}) of the MMC is illustrated in Equation (7). N_{level} is the number of levels of MMC and $V_{SM,avg}$ is the average submodule voltage.

$$V_{DC} = N_{level} \times v_{SM,avg}^2 \tag{7}$$

Moreover, each arm of MMC-HVDC has the stored energy as shown as follows:

$$E_{arm,avg} = \frac{1}{2} C_{SM} v_{SM,avg}^2 \times N_{SM} \tag{8}$$

The total number of the submodule in MMC is 6 N_{SM} because MMC has six arms. The stored energy in MMC is revealed in Equation (9).

$$W_{MMC} = \frac{1}{2} C_{SM} v_{SM,avg}^2 \times (6N_{SM}) \tag{9}$$

So,

$$\frac{6C_{SM} N_{SM} v_{SM,avg}}{S_{MMC}} . \frac{dv_{SM,avg}}{dt} = \Delta P_2 \left(pu\right) \tag{10}$$

This equation shows that any change in direct voltage changes the energy stored in the capacitors. The power of the synchronous machine in Equation (5) can be equal to the capacity of the capacitor in Equation (10).

$$\Delta P_1 \left(pu\right) = \Delta P_2 \left(pu\right) \tag{11}$$

Therefore ΔP_1 can be added to the reference active power obtained from the droop controller of the proposed controller that is shown in Figure 1 It should be noted that any change in power reference leads to voltage changes, and therefore it can change the level of energy stored in the sub-modules of the MMC. In the proposed method, the frequency of the AC side is measured and is combined with the inertia coefficient which is calculated in Equation (5). Simultaneously, damping signals from DC-PSS are injected into the droop controller loop. Then, both of these signals will be compared with the measured DC power to be applied to the power controller as a power reference. As it is shown in Figure 1 one loop is receiving frequency error feedback from the AC side and another loop is taking direct voltage error from the DC side, both at the same converter station. However, the voltage signal is converted to a power signal through the droop controller, which means that they do not conflict with each other. By applying this control method, in the initial moments of fault, the inertia is emulated through frequency changes, in the direct voltage and it will prevent sudden changes in the hybrid HVAC/HVDC network. Since, using this method, frequency changes act as energy storage for direct voltage.

2.2 | DC-PSS

The presence of relatively large DC reactors, which are an essential part of DC breakers, have major implications for HVDC grid stability. In the transient conditions, direct voltages of the HVDC grid will be regulated by the action of the V–P droop control equipped with the DC-PSS to remove the instabilities of power coming from other stations. Figure 2 shows a straight structure of a DC-PSS, as exposed in this figure, in each HVDC grid, the power balance index, is the local measured voltage used as the input [32].

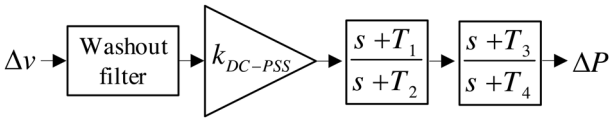

FIGURE 2 The DC-PSS structure

3 | SMALL SIGNAL ANALYSIS

If the modal analysis (small-signal analysis) is used to investigate the impact of the proposed control method on the system stability, the linearized model of the power system can be expressed in state-space form as [20]:

$$\Delta \dot{x} = \boldsymbol{A}\Delta x + \boldsymbol{B}\Delta u \tag{12}$$

where Δx and $\boldsymbol{A}$ denote the state vector and the state space matrix correspondingly, Δu and $\boldsymbol{B}$ signify the input vector and input matrix correspondingly.

3.1 | MMC modelling

Analysis of the proposed method for applying MMC in the system requires understanding the dynamic behaviour of the power converter and its controller. The arm switching function model of an MMC-HVDC converter is proper for hybrid AC/DC systems analysis. It should be noted that, in this case, IGBTs arrangement is different, being grouped in submodules along with DC capacitors, also, their switching frequencies in comparison with converters with two- or three-level power is lower [33].

The control system of MMC converters, generally, has a cascade structure. The external controller of the power converter is usually based on the vector controller. This part of the controller is responsible for controlling the input and output variables of the AC/DC converter (AC or DC voltage and active or reactive power). The higher-level controller has a lower bandwidth in contrast with its lower-level controller. In an ideal separate performance and well-designed cascade control, the higher-level control operates 6–10 times slower compared to the next lower-level control loop. Figure 3 illustrates the control diagram of the arm switching function model of an MMC. The arm switching function model of an MMC has the most applications in terms of accuracy and velocity of calculations and it is an appropriate model for transient analysis [33]. However, the detailed IGBT-based model of MMC, due to its very low computational speed and high accuracy is used only to investigate and estimate losses. Also, the AVM MMC model is not used in transient DC studies, since it has an incorrect response to DC side faults [33].

In this type of modelling, considering the concept of a half-bridge converter switching performance. The dynamics of such a system can be examined in several steps as follows.

- Internal variables modelling of an MMC
- DC side electrical modelling
- AC side electrical modelling and PLL structure

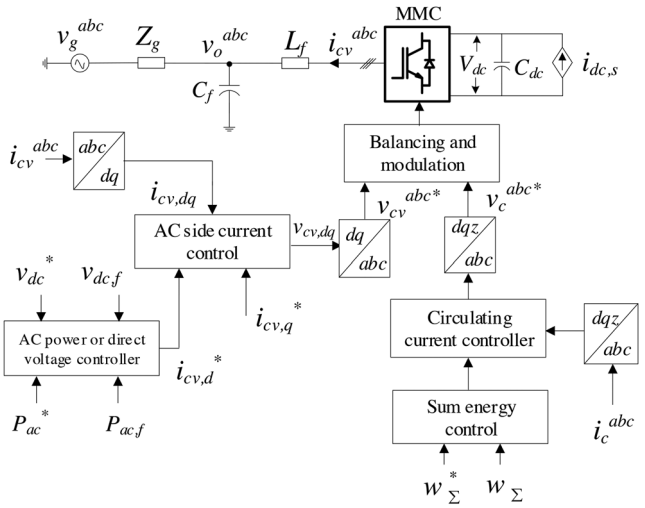

FIGURE 3 MMC model including its control structure

3.1.1 | Internal variables modelling of an MMC

The internal circulating current of the zero-sequence is controlled by the internal loop PI controller to determine the value of the corresponding reference voltage $v_{c,z}^*$. The control system is designed in such a way that k_{ffdc} as the feedforward loop performance coefficient has a number between zero and one, if the controller has a feedforward loop, the k_{ffdc} value is one and otherwise it is zero.

$$\begin{aligned} \mathrm{v}_{\mathrm{c,z}}^* &= -k_{\mathrm{pc,z}}\left(i_{\mathrm{c},\Sigma}^* - i_{\mathrm{c,z}}\right) - k_{\mathrm{ic,z}}\xi_{\mathrm{z}} + k_{ffdc}v_{\mathrm{dc}} \\ \frac{d}{dt}\xi_{\mathrm{z}} &= \mathrm{i}_{\mathrm{c,z}}^* - i_{\mathrm{c,z}} \end{aligned} \tag{13}$$

By using voltage compensated modulation, the product-induced nonlinearity between the insertion indices and the total arm voltage, and the effect of capacitor voltage fluctuations on the internal control loops, are effectively compensated. Therefore, these effects can be removed from the system model and the conduction voltages of the ac side currents and the zero sequence current can be assumed to be equal to their reference values when modelling the equations of the electrical circuit and the corresponding control loops [34]. With only the aggregated energy sum and the zero sequence circulation current retained as the internal variables of the MMC, the modelled part of the control system from Figure 3 includes two PI controller loops. As an outer control loop, a PI controller, controls the aggregated energy in order to provide a zero-sequence circulating current reference. The operation of this controller is shown in Equation (14), where, $k_{pw,\Sigma}$ and $k_{iw,\Sigma}$ are the gains of the PI controller.

$$\begin{aligned} i_{c,z}^* &= k_{pw,\Sigma}\left(w_\Sigma^* - w_\Sigma\right) + k_{iw,\Sigma}k_\Sigma \\ \frac{d}{dt}k_\Sigma &= w_\Sigma^* - w_\Sigma \end{aligned} \tag{14}$$

3.1.2 | DC side electrical modelling

State variables of DC side electrical modelling is shown in the following equations. Where the crossover frequency of the low-pass filter is shown by ω_{dcf}. The control system is such that the AC power defined by Equation (16) passes through the low-pass filter before being used in the power control loop as shown in Equation (15).

$$\begin{aligned} \frac{d}{dt} v_{dc} &= \frac{\omega_b}{C_{dc}} \left(i_{dc,s} - 4i_{cz}\right) \\ \frac{d}{dt} v_{dc,f} &= \omega_{dc,f} \left(v_{dc} - v_{dc,f}\right) \end{aligned} \tag{15}$$

$$\begin{aligned} P_{ac} &= v_{o,d}\, i_{cv,d} + v_{o,q} i_{cv,q} \\ \frac{d}{dt} P_{ac,m} &= \omega_{pac} \left(P_{ac} + P_{ac,m}\right) \end{aligned} \tag{16}$$

The reference current $i^*_{cv,d}$ is defined by PI controller of power and a direct voltage droop determines the AC power reference as it is expressed in Equation (17).

$$\begin{aligned} i^*_{cv,d} &= k_{pp,ac} \left(P^*_{ac} - P_{ac,m}\right) + k_{ip,ac}\rho \\ \frac{d}{dt}\rho &= P^*_{ac} - P_{ac,m} \\ P^*_{ac} &= k_{droop} \left(v^*_{dc} - v_{dc,f}\right) + P^{ref}_{ac} \end{aligned} \tag{17}$$

3.1.3 | AC side electrical modelling and PLL structure

The current controller loops and phase-locked loop (PLL), relevant to the AC side of the MMC converter, can be modelled like the AC side modelling of VSC converters [33]. In the following equations, i_{cv} is the power converter side current, i_o is the grid side current and v_o is equivalent capacitor voltage.

$$\frac{d}{dt} i_{cv} = -\left(\frac{\left(\frac{r_a}{2} + r_f\right)\omega_b}{\frac{L_a}{2} + L_f} + j\omega_g\omega_b\right) i_{cv} + \frac{\omega_b}{\frac{L_a}{2} + L_f} v_{cv} - \frac{\omega_b}{\frac{L_a}{2} + L_f} v_o \tag{18}$$

$$\begin{aligned} \frac{d}{dt} v_o &= -j\omega_g\omega_b v_o + \frac{\omega_b}{C_f} i_{cv} - \frac{\omega_b}{C_f} i_o \\ \frac{d}{dt} i_o &= -\left(j\omega_g\omega_b + \frac{r_g\omega_b}{L_g}\right) i_o - \frac{\omega_b}{C_f} v_g + \frac{\omega_b}{C_f} v_o \end{aligned} \tag{19}$$

where ω_g is the per-unit grid frequency and L_a, r_a, L_f, r_f, l_g, r_g, C_f are the resistances, capacitance, and inductances of the system.

The AC side currents of the power converter are controlled by decoupled PI controllers corresponding to the d and q axes. The equations of these controllers are defined by Equations (20) and (21).

$$\begin{aligned} & k_{ffv} v_o - v^*_{AD} + k_{pc}\left(i^*_{cv} - i_{cv}\right) + k_{ic}\gamma + jL_f\omega_{PLL} i_{cv} \\ & \frac{d}{dt}\gamma = i^*_{cv} - i_{cv} \end{aligned} \tag{20}$$

$$\begin{aligned} v^*_{AD} &= k_{AD}\left(v_o - \varphi\right) \\ \frac{d}{dt}\varphi &= \omega_{AD}\left(v_o - \varphi\right) \end{aligned} \tag{21}$$

The k_{ffv} as the coefficient of performance of the feedforward loop has a number between zero and one if the controller has a feedforward loop of v_o, the value of k_{ffv} is one and otherwise it is zero. Also, v^*_{AD} is used to eliminate LC oscillation. In Equation Equation (21), φ is the state of a filter.

PLL configuration contains a PI controller. The linear equations of PLL are described in Equation (22) [35].

$$\begin{aligned} \frac{d}{dt}\theta_{PLL} &= k_{p,PLL}\, v_{o,q} + x_{PLL} \\ \frac{d}{dt} x_{PLL} &= v_{o,q} \end{aligned} \tag{22}$$

Therefore, the matrix of state variables is illustrated in Equation (23) and the input matrix is expressed in Equation (24).

$$\begin{aligned} \boldsymbol{x_j} = [&v_{od}\ v_{oq}\ i_{cv,d}\ i_{cv,q}\ \gamma_d\ \gamma_q\ i_{o,d}\ i_{o,q}\ \varphi_d\ \varphi_q\ v_{dc} \\ &v_{PLL,d}\ v_{PLL,q}\ v_{dc,f}\ \rho\ p_{ac,m}\ i_{c,z}\ k_\Sigma\ \xi_z\ w_z]^T \end{aligned} \tag{23}$$

$$\boldsymbol{u_j} = \left[v^{ref}_{dc}\ P^{ref}_{ac}\ i^*_{cv,q}\ \left|v_g\right|\ i_{dc,s}\ w^*_\Sigma\right]^T \tag{24}$$

As it is shown in Equation (25), The matrices related to $\Delta v_{DC(j)}$ and $\Delta i_{dc(j)}$ are mined to enable the integration of the MMC model and the HVDC grid.

$$\begin{aligned} \dot{\boldsymbol{x}}_j &= \boldsymbol{A_j}\,\boldsymbol{x_j} + \boldsymbol{B_{dj}}\boldsymbol{xd_j} + \left[\boldsymbol{B_{jG}}\ \boldsymbol{B_j}\right]\begin{bmatrix}\Delta i_{dc(j)} \\ \Delta P^*_j\end{bmatrix} \\ \Delta v_{DC(j)} &= \boldsymbol{C_{jG}}\, x_j \end{aligned} \tag{25}$$

3.2 | DC line model

The conventional π-section model of a line accurately shows the cable behaviour only at a single point of the frequency domain. In the π-section model, increasing the number of π-sections improves hyperbolic factors, but does not necessarily lead to a good approximation of the actual behaviour of the cable because it does not allow the frequency dependence of the distributed parameters to be considered [36]. Instead, the frequency-dependent π model can be used to modelling the

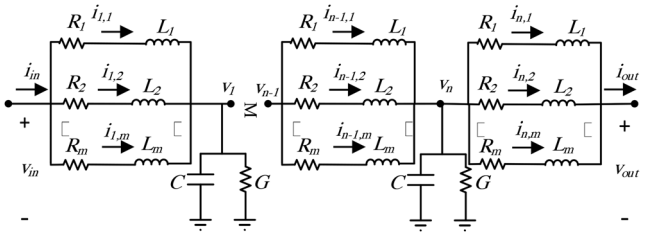

FIGURE 4 FD-π model of the lines

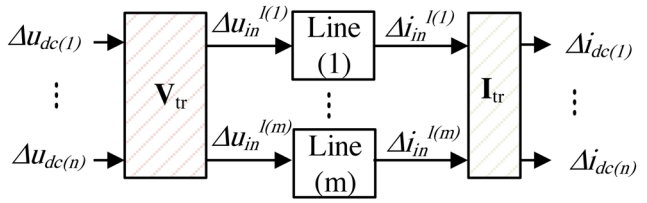

FIGURE 5 Integrating lines with power converters of HVDC grid

behaviour of cables in a specific frequency range. The FD- π model consists of a lumped circuit with parallel *R-L* branches in each section of the π model of the line. The accuracy and validity of the FD- π model are determined by the number of sections of the π model and the number of parallel branches in each section.

To model the line based on FD-π, first the line is divided into *n* sections. The number of sections is determined by the length of the line and the frequency range to be interested. Then the number of parallel lines is considered and specified.

Figure 4 shows the line model based on FD-π [37]. The number of the parallel branch is showed by *m*.

Figure 5 displays the construction of a DC network with lines (*m*) and converters (*n*). A schematic of a MIMO system for stability investigation in the HVDC grid is shown in Figure 6 Understudy HVDC grid includes 5-terminal. The terminal power reference is the input signal and the voltage is the output signal.

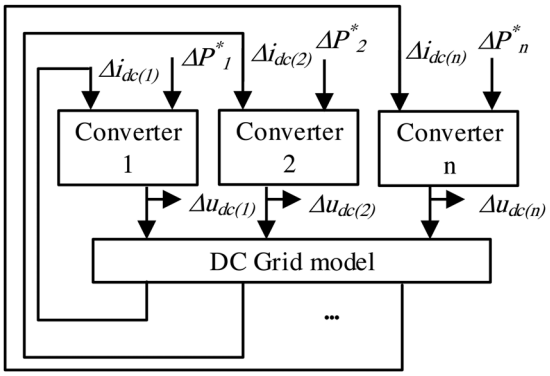

FIGURE 6 Schematic of HVDC MIMO grid

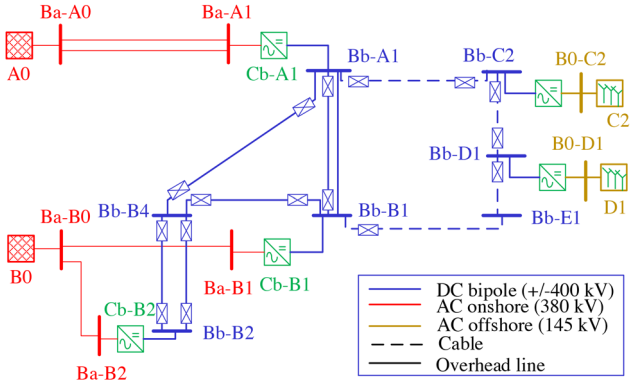

FIGURE 7 Cigré DCS3 test HVDC grids

4 | SIMULATION RESULTS

4.1 | Understudy network

The diagram of the under-study network is shown in Figure 7 In this paper, Cigré DCS3 test grid is used to analyse the proposed method.

This grid consists of four AC areas that are connected via a 5-terminal bipolar power converter station [38]. The HVDC transmission lines are considered by the FD-π model.

4.2 | Optimization parameters of DC-PSS

Stabilizer parameters must be adjusted before the optimal placement of the inertia and DC-PSS emulation loops to reduce the value of the objective function Equation (26).

$$Error = \sum_{b=1}^{n} \left(\int_0^t t \left(\left| \Delta V_{dc_b} \right| + \left| \Delta P_b \right| \right) dt \right) \tag{26}$$

Integration of the area under the curve of oscillation of direct voltage and the area under the curve of oscillation of active power for n AC/DC bus during specified time is exposed in Equation (26). The main contribution of this paper is to facilitate inertia emulation based on the *P*–*V* droop control and DC-PSS of an MMC. So, the frequency stability has been considered in parameters optimization through active power variations in Equation (26). According to this equation, if there is no fault or malfunction in the system, the Error function will be zero. In this paper, the PSO algorithm is employed to determine the DC-PSS parameters based on Equation (26) [39]. The procedure of solving the optimization problem by PSO algorithm is such that at the beginning and at the specified time, a fault is applied, the zone below the DC voltage oscillation curve and active power oscillation curve is calculated for all AC/DC buses and finally, all calculated areas are used as performance criteria in Equation (26). Then, the goal is deliberated.

TABLE 1 Optimization result for DC-PSS by PSO algorithm following a fault in BA-A0

Parameter	K_{DC}	T_1 (s)	T_2 (s)	T_3 (s)	T_4 (s)
Optimal value	131.2	0.0184	0.0107	0.00132	0.007
Minimum value	1	0.01	0.01	0.01	0.01
Maximum value	1000	0.1	0.1	0.1	0.1

TABLE 2 Optimization result for DC-PSS by PSO algorithm following a fault in BA-B0

Parameter	K_{DC}	T_1 (s)	T_2 (s)	T_3 (s)	T_4 (s)
Optimal value	131.1	0.0174	0.0105	0.00131	0.0072
Minimum value	1	0.01	0.01	0.01	0.01
Maximum value	1000	0.1	0.1	0.1	0.1

However, the design problem of DC-PSS has the following constraints:

$$K_{DC,min} \le K_{DC} \le K_{DC,max} \tag{27}$$

$$T_{1,min} \le T_1 \le T_{1,max} \tag{28}$$

$$T_{2,min} \le T_2 \le T_{2,max} \tag{29}$$

$$T_{3,min} \le T_3 \le T_{3,max} \tag{30}$$

$$T_{4,min} \le T_4 \le T_{4,max} \tag{31}$$

Initially, PSO starts with a population of random solutions and then searches for the global optimal solution through continuous up-gradation of the populations.

The optimum parameters of DC-PSS and limitation of each parameter with 120 repetitions following a three-phase fault in Ba-A0 place with a duration of 150 ms are presented in Table 1 The optimum parameters of DC-PSS and limitation of each parameter with 120 repetitions following a three-phase fault in Ba-B0 place with a duration of 150 ms are presented in Table 2 The optimum parameters of DC-PSS and limitation of each parameter with 120 repetitions following a three-phase fault in Ba-B1 place with a duration of 150 ms are presented in Table 3

For robustness of the solutions, the obtained values of parameters of the Genetic Algorithm (GA) and the PSO algorithm are compared following several faults including a three-phase fault with a duration of 150 ms in Ba-A0, Ba-B0, and Ba-B1. The results of this comparison are shown in Table 4 As the table shows, the proposed PSO algorithm achieves a better response than the GA algorithm, it also has a faster response and fewer repetitions.

TABLE 3 Optimization result for DC-PSS by PSO algorithm following a fault in BA-B1

Parameter	K_{DC}	T_1 (s)	T_2 (s)	T_3 (s)	T_4 (s)
Optimal value	131.2	0.0183	0.0108	0.00131	0.0069
Minimum value	1	0.01	0.01	0.01	0.01
Maximum value	1000	0.1	0.1	0.1	0.1

TABLE 4 Comparison of the parameters obtained from two algorithm

	K_{DC}	T_1 (s)	T_2 (s)	T_3 (s)	T_4 (s)	Repetition
	Ba-A0					
	131.1	0.0180	0.0105	0.00133	0.066	95
PSO	Ba-B0					
	131.8	0.0179	0.0103	0.00128	0.068	120
	Ba-B1					
	132.2	0.0184	0.0109	0.00130	0.069	126
	Ba-A0					
	132.3	0.0179	0.0104	0.00134	0.0067	200
GA	Ba-B0					
	132.1	0.0177	0.0105	0.00138	0.0065	200
	Ba-B1					
	132.9	0.0181	0.0105	0.00129	0.0067	200

4.3 | Optimal placement of the proposed method

The participation factor (PF) method is employed in Cigré DCS3 system to determine the appropriate location of the inertia emulation loop and DC-PSS.

Important data about the MIMO system can be reveals by the method of singular value [40], so, it is employed in multivariate systems. Singular value analysis calculates the gain among the reference of the power of a particular power converter and voltage of terminals. The plane of the singular value according to Equation (12) shows the gains between the norm of Euclidean of the input vector and its output in the range of frequency [41]. The terminal with a bigger singular value in a particular frequency range can be selected as a decent place for DC-PSS and inertia emulation loops due to the sensitivity to power change in this place. The data of the system are given in Table 5

Figure 8 shows the diagram of poles and zeros of the small-signal control model with different values of H.

As shown in Figure 8 the system is generally stable and all poles are on the left side of the complex plane. This figure shows that by increasing the inertia constant value from zero to 4 s,

TABLE 5 Parameters of power converters

Value	Parameter
160 per arm	N_{SM}: Number of submodules
3.5 mF	C: Submodule capacitance
4	H: Emulated inertia time constant
50 Hz	f_o: Rated frequency

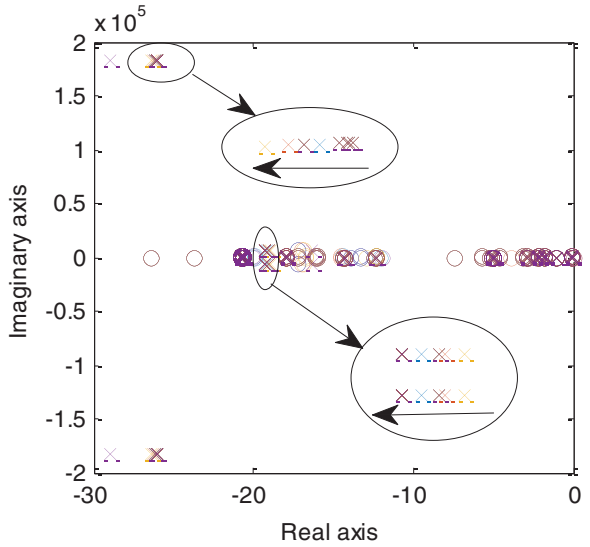

FIGURE 8 Zeroes and dominant poles between $H = 0$ to $H = 4$ ($N = 1$, $C = 3.5$ mF)

conjugate poles of the system move to the zero axes, but the poles located on the horizontal axis, move farther from the axis. The singular values between the voltage vector and power of specific terminals for a closed-loop model are shown in Figure 9

Table 7 shows the normalized participation factors associated with eigenvalues that bigger than 0.2 and it shows the state

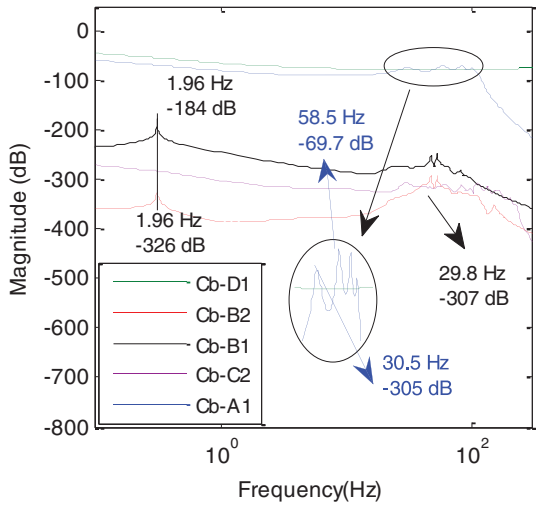

FIGURE 9 Singular value plans of the closed-loop models for direct voltages of the terminal with k_{droop} of Cb-B1 = 0.25; k_{droop} of Cb-B2 = 0.52

TABLE 6 Frequency, damping related to the eigenvalue for the oscillatory modes

	Inertia loop and DC-PSS in Cb-B1	Inertia loop and DC-PSS in Cb-B2
Eigen value	$-2.27 \pm 18.95i$	$-1.08 \pm 17.36i$
Damping ratio	0.119	0.0620
Frequency (Hz)	1.51	2.76
Eigen value	$-19 \pm 110i$	$-23 \pm 113i$
Damping ratio	0.17	0.12
Frequency (Hz)	17.50	17.98

TABLE 7 Normalize Participation factors for all buses

Eig.	State variable	Normalized PF	Bus
−10.5	$\Delta e_d, \Delta v_d, \Delta x_{id}, \Delta u_{dc}$	0.32, 0.95, 0.221, 0.99	Cb-B1
	$\Delta v_d, \Delta x_{id}, \Delta u_{dc}, \Delta i_{l\text{-}dc}$	0.12, 0.47, 0.61, 0.92	Cb-B2
	$\Delta e_d, \Delta v_d, \Delta x_{id}, \Delta u_{dc}$	0.73, 0.81, 0.02, 0.24	Cb-A1
	Δx_{id}	0.33	Cb-C2
	$\Delta u_{dc}, \Delta i_{l\text{-}dc}$,	0.382, 0.36	Cb-D1
-1.39 ± 18.7i	$\Delta e_d, \Delta i_{line,d}, \Delta v_d$,	1, 0.91, 0.51	Cb-B2
−2	$\Delta v_d, \Delta e_d$,	0.41, 0.62	Cb-A1
	Δe_d,, Δx_{id}, Δv_d	1, 0.892, 0.981	Cb-B1

variables and their related bus. Table 7 shows that the insecurity mode has special values associated with Cb-B1 concerning the participation coefficient. This demonstrates the Cb-B1 that used droop is a proper place to install the proposed controller to compare the converter without a droop controller.

The frequency oscillation and damping ratio eigenvalues of the system according to the location of the inertia loop and DC-PSS are shown in Table 3 This table shows that the system with inertial loop and DC-PSS in Cb-B1 has a higher damping ratio in compare comparison with the network with inertia loop and DC-PSS in Cb-B1.

Table 6 revealed the participation factors following the low frequency very weak damply terminal modes, according to its voltage. For each of the finite eigenvalues that correspond to the corresponding state variables of the system model, the PF participation coefficient is written.

4.4 | Investigation of the proposed method for the understudy network

In this part of the paper, the effect of the inertia emulation loop and DC-PSS alongside with droop controller on the Cigré DCS3 grid is investigated under three scenarios. These scenarios are examined as follows:

Case 1: This scenario is reducing the power output of the Cb-A1 bus at 3 s.

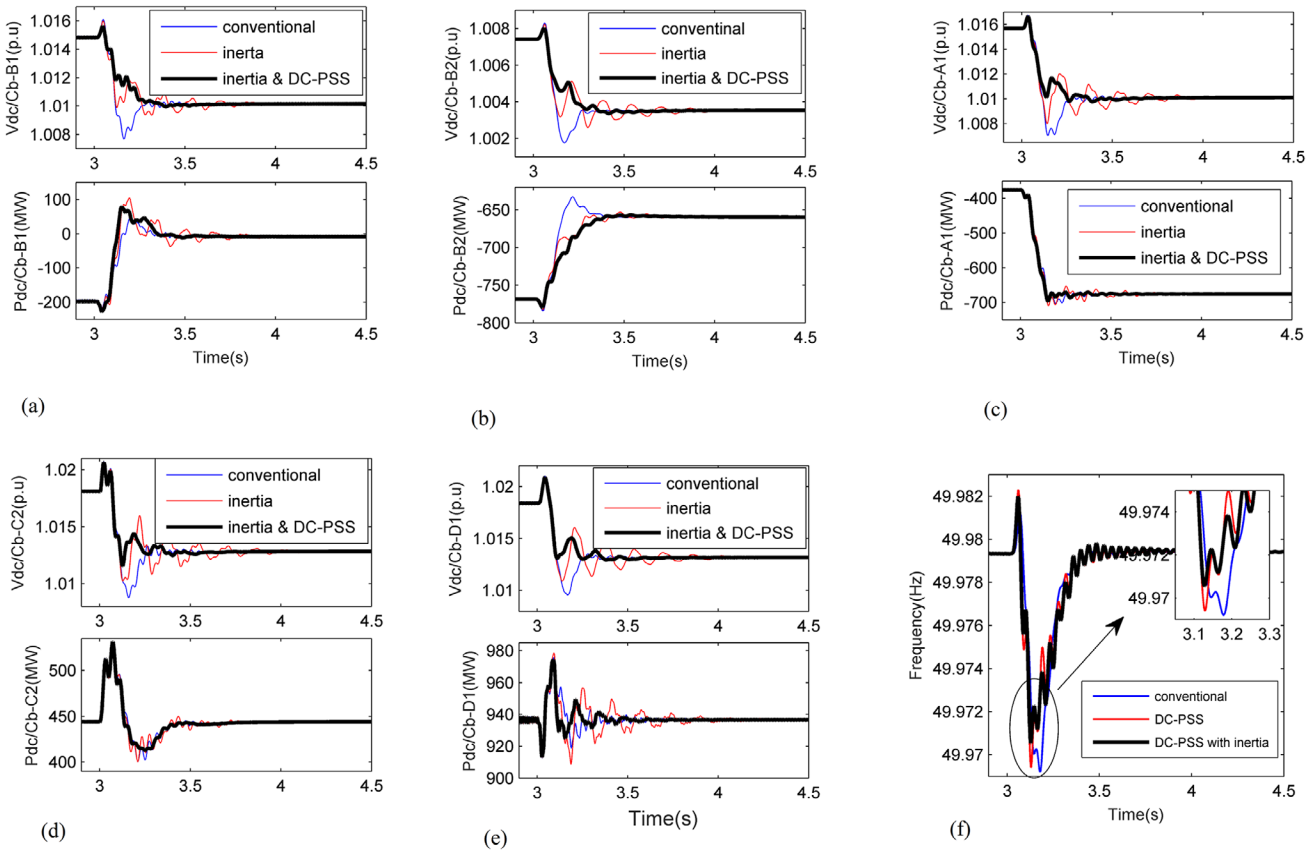

FIGURE 10 Direct voltage and DC power after power change in Cb-A1; (a) Cb-B1; (b) Cb-B2; (c) Cb-A1; (d) Cb-C2; (e) Cb-D1; (f) frequency in Cb-A1

Case 2: This scenario is 3 phase fault with a duration of 3–3.5 s in Ba-A0.

Case 3: This scenario is 3 phase fault with a duration of 3–3.15 s in Ba-B0.

In these simulations, the inertia control loop is applied to the Cb-B1 bus converter. DC voltage and active power of the Cb-B1, Cb-B2, Cb-A1, Cb-C2, Cb-D1 by utilizing DC-PSS, inertia emulation loop.

Case1: This scenario is reducing the power output of the Cb-A1 bus at 3 s: As shown in Figure 10a at 3 s as the power output of Cb-A1 decreases, the voltage in the Cb-B1 changes from 1.015 p.u. to 1.01. At the same time, the output power of this bus is changing from about −200 MW to about −10 MW. As shown in this figure, by adopting the inertia control loop and DC-PSS, the power fluctuation is eliminated and it slowly reaches to steady-state condition without any drop or a sudden increase in its signal. Also, by using DC-PSS alongside the inertia emulation loop, the dynamic performance of DC voltage can be improved. Figure 10b shows the simulation results under the previous scenario on reducing power production of the Cb-B2 bus. The results for this bus also confirm that the stability of the output power of Cb-B2 can be improved by using both DC-PSS and inertia emulation.

As shown in Figure 10b in addition to the output power, the DC voltage does not decrease or increase abruptly using the inertial loop and slowly reaches its final value. The simulation results for the Cb-A1 bus also show in Figure 10c

It should be noted that the proposed method has a good performance in power-sharing and does not impair the performance of the droop controller. As it is shown in Figure 10d e, the simulations for these buses repeat the same previous results, except that the controller for these buses is a power controller. The frequency of the grid under the conventional method, DC-PSS, and by using DC-PSS with inertia is shown in Figure 10f As this figure shows, the frequency using DC-PSS equipped with inertia has a lower peak.

Case2: This scenario is 3 phase fault with a duration of 3–3.5 s at Ba-A0: Figure 11a displays the voltage signal of Cb-A1 under three-phase short-circuit at Ba-A0 from 3 to 3.5 s.

In the current part, to investigate the impact of DC-PSS, three Cb-B1 basses as the optimal location and Cb-B2 bass as the second optimal location according to Tables 3 and 4 and the Cb-A1 bus arbitrarily designated. Also, Figure 11b shows the fluctuations of the frequency of the AC side of Cb-B1 power converter. As shown in Figure 11b the use of DC-PSS equipped with inertia, under 3 phase fault with a duration of 3–3.5 s at Ba-A0, has also contributed to AC frequency stability. This figure shows that the DC-PSS and the inertia emulation loop located in Cb-B1 as the optimal location can damp oscillations under fault conditions.

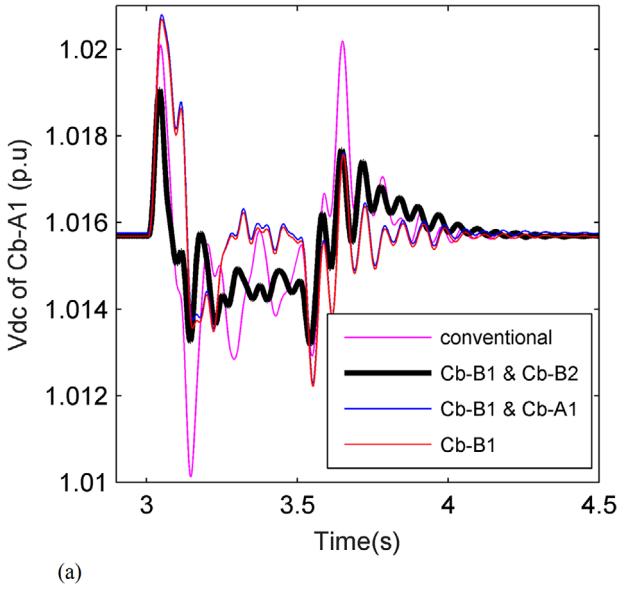

(a)

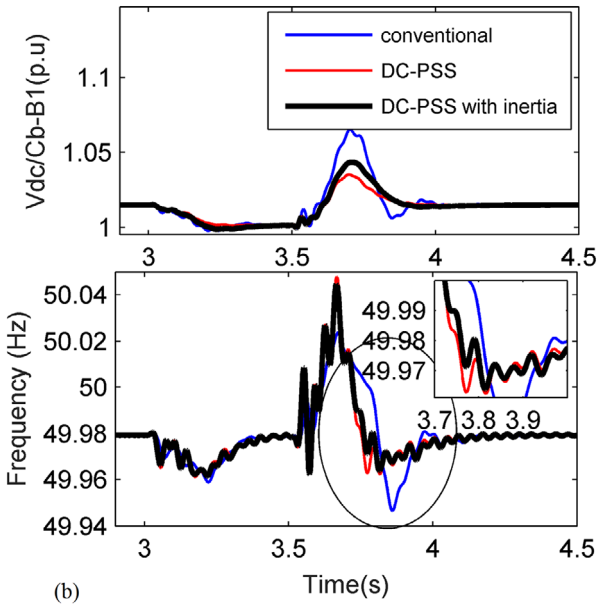

(b)

FIGURE 11 (a) Direct voltage of Cb-A1 after an incident fault in Ba-A0; (b) frequency of the grid after an incident fault in Ba-A0

TABLE 8 The area under the frequency fluctuation curve for *n* DC buses with inertia emulation loop and without inertia

Cb-B1, Cb-B2	Cb-B1, Cb-A1	Cb-B1	Conventional
0.097	0.105	0.109	0.162

Table 8 shows the value of the objective function (26) under three short-circuit in Ba-A0 to guarantee the correctness of the responses. This table demonstrates that a system that used DC-PSS and an inertia emulation loop in the optimal location responds better than other conditions.

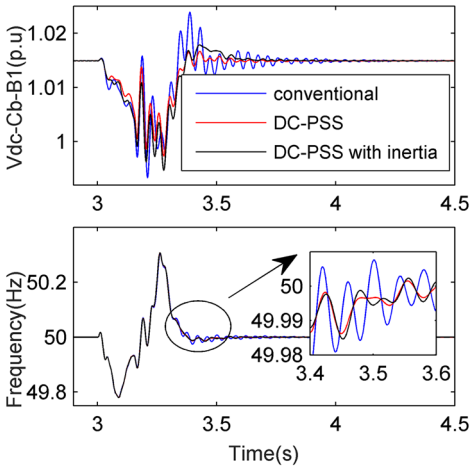

FIGURE 12 Direct voltage of Cb-A1 after an incident fault in Ba-B0 and frequency of the grid after an incident fault in Ba-B0

Case3: This scenario is 3 phase fault with a duration of 3–3.15 s at Ba-B0: Figure 12 shows the fluctuations of the frequency of the AC side of the Cb-A1 power converter. As shown in Figure 12 the use of DC-PSS equipped with inertia, under 3 phase fault with a duration of 3–3.15 s at Ba-B0, has also contributed to AC frequency stability. This figure shows that the DC-PSS and the inertia emulation loop located at Cb-B1 as the optimal location can damp oscillations under fault conditions.

5 | CONCLUSION

Direct voltage oscillations, lack of inertia, frequency fluctuations and generation balance, demand, and power losses jeopardize the stable operation of the HVAC/HVDC grids. To address these issues, in this paper, a method is proposed that enables the power converters to emulate system inertia for frequency stability enhancement in the events of direct power fluctuations and operate alongside the DC-PSS and droop controller. This method prevents sudden fluctuations in frequency, power, and direct voltage and it has similar behaviour to synchronous generators against abrupt changes. This paper shows through various analyses and simulations that the introduced method significantly improves the overall stability of the system.

FUNDING

None

CONFLICT OF INTEREST

The authors confirms that this article content has no Conflicts of Interest

PERMISSION TO REPRODUCE MATERIALS FROM OTHER SOURCES

None

DATA AVAILABILITY STATEMENT

Data sharing is not applicable to this article as no new data were created or analyzed in this study.

ORCID

Hassan Moradi CheshmehBeigi https://orcid.org/0000-0002-4802-6117

REFERENCES

1. Cardiel-Alvarez, M.A., Arnaltes, S., Rodriguez-Amenedo, J.L., Nami, A.: Decentralized control of offshore wind farms connected to diode-based HVDC links. IEEE Trans. Energy Convers. 33(3), 1233–1241 (2018)
2. Zhu, J., Booth, C.D., Adam, G.P., Roscoe, A.J., Bright, C.G.: Inertia emulation control strategy for VSC-HVDC transmission systems. IEEE Trans. Power Syst. 28(2), 1277–1287 (2012)
3. Rakhshani, E., Luna, A., Rouzbehi, K., Rodriguez, P., Etxeberria-Otadui, I.: Effect of VSC-HVDC on load frequency control in multi-area power system. In: *2012 IEEE Energy Conversion Congress and Exposition (ECCE)*, Raleigh, NC, USA, pp. 4432–4436 (2012)
4. Nomura, S., Tsutsui, H., Tsuji-Iio, S., Shimada, R.: Flexible power interconnection with SMES. IEEE Trans. Appl. Supercond. 16(2), 616–619 (2006)
5. Haileselassie, T.M., Uhlen, K.: Impact of DC line voltage drops on power flow of MTDC using droop control. IEEE Trans. Power Syst. 27(3), 1441–1449 (2012)
6. Sarlette, A., Dai, J., Phulpin, Y., Ernst, D.: Cooperative frequency control with a multi-terminal high-voltage DC network. Automatica 48(12), 3128–3134 (2012)
7. Dai, J., Phulpin, Y., Sarlette, A., Ernst, D.: Coordinated primary frequency control among non-synchronous systems connected by a multi-terminal high-voltage direct current grid. IET Gener. Transm. Distrib. 6(2), 99–108 (2012)
8. Li, Y., Zhou, Y., Liu, F., Cao, Y., Rehtanz, C.: Design and implementation of delay-dependent wide-area damping control for stability enhancement of power systems. IEEE Trans. Smart Grid 8(4), 1831–1842 (2016)
9. Cheema, K.M.: A comprehensive review of virtual synchronous generator. Int. J. Electr. Power Energy Syst. 120, 106006 (2020)
10. Jahan, E., Hazari, M.R., Muyeen, S., Umemura, A., Takahashi, R., Tamura, J.: Primary frequency regulation of the hybrid power system by deloaded PMSG-based offshore wind farm using centralised droop controller. J. Eng. 2019(18), 4950–4954 (2019)
11. Zhang, C., Wei, Y.-L., Cao, P.-F., Lin, M.-C.: Energy storage system: Current studies on batteries and power condition system. Renewable Sustainable Energy Rev. 82, 3091–3106 (2018)
12. Rouzbehi, K., Candela, J.I., Gharehpetian, G.B., Harnefors, L., Luna, A., Rodriguez, P.: Multiterminal DC grids: Operating analogies to AC power systems. Renewable Sustainable Energy Rev. 70, 886–895 (2017)
13. Liu, H., Chen, Z.: Contribution of VSC-HVDC to frequency regulation of power systems with offshore wind generation. IEEE Trans. Energy Convers. 30(3), 918–926 (2015)
14. Kayikçi, M., Milanovic, J.V.: Dynamic contribution of DFIG-based wind plants to system frequency disturbances. IEEE Trans. Power Syst. 24(2), 859–867 (2009)
15. Conroy, J.F., Watson, R.: Frequency response capability of full converter wind turbine generators in comparison to conventional generation. IEEE Trans. Power Syst. 23(2), 649–656 (2008)
16. Zhu, J., Guerrero, J.M., Hung, W., Booth, C.D., Adam, G.P.: Generic inertia emulation controller for multi-terminal voltage-source-converter high voltage direct current systems. IET Renewable Power Gener. 8(7), 740–748 (2014)
17. Zhang, W., Rouzbehi, K., Luna, A., Gharehpetian, G.B., Rodriguez, P.: Multi-terminal HVDC grids with inertia mimicry capability. IET Renewable Power Gener. 10(6), 752–760 (2016)
18. Ashabani, M., Mohamed, Y.A.-R.I.: Novel comprehensive control framework for incorporating VSCs to smart power grids using bidirectional synchronous-VSC. IEEE Trans. Power Syst. 29(2), 943–957 (2013)
19. Wang, W., Li, Y., Cao, Y., Häger, U., Rehtanz, C.: Adaptive droop control of VSC-MTDC system for frequency support and power sharing. IEEE Trans. Power Syst. 33(2), 1264–1274 (2017)
20. Wang, W., Barnes, M., Marjanovic, O., Cwikowski, O.: Impact of DC breaker systems on multiterminal VSC-HVDC stability. IEEE Trans. Power Delivery 31(2), 769–779 (2015)
21. Poolla, B.K., Bolognani, S., Dörfler, F.: Optimal placement of virtual inertia in power grids. IEEE Trans. Autom. Control 62(12), 6209–6220 (2017)
22. Adib, A., Mirafzal, B., Wang, X., Blaabjerg, F.: On stability of voltage source inverters in weak grids. IEEE Access 6, 4427–4439 (2018)
23. Lu, M., Al-Durra, A., Muyeen, S., Leng, S., Loh, P.C., Blaabjerg, F.: Benchmarking of stability and robustness against grid impedance variation for LCL-filtered grid-interfacing inverters. IEEE Trans. Power Electron. 33(10), 9033–9046 (2017)
24. Kim, B.-H., Sul, S.-K.: Stability-oriented design of frequency drift anti-islanding and phase-locked loop under weak grid. IEEE J. Emerg. Sel. Top. Power Electron. 5(2), 760–774 (2016)
25. Zhang, X., Xia, D., Fu, Z., Wang, G., Xu, D.: An improved feedforward control method considering PLL dynamics to improve weak grid stability of grid-connected inverters. IEEE Trans. Ind. Appl. 54(5), 5143–5151 (2018)
26. Chen, X., Zhang, Y., Wang, S., Chen, J., Gong, C.: Impedance-phased dynamic control method for grid-connected inverters in a weak grid. IEEE Trans. Power Electron. 32(1), 274–283 (2016)
27. Li, X., Fang, J., Tang, Y., Wu, X., Geng, Y.: Capacitor-voltage feedforward with full delay compensation to improve weak grids adaptability of LCL-filtered grid-connected converters for distributed generation systems. IEEE Trans. Power Electron. 33(1), 749–764 (2017)
28. Li, C., Chaudhary, S.K., Savaghebi, M., Vasquez, J.C., Guerrero, J.M.: Power flow analysis for low-voltage AC and DC microgrids considering droop control and virtual impedance. IEEE Trans. Smart Grid 8(6), 2754–2764 (2016)
29. Mahmood, H., Michaelson, D., Jiang, J.: Accurate reactive power sharing in an islanded microgrid using adaptive virtual impedances. IEEE Trans. Power Electron. 30(3), 1605–1617 (2014)
30. Vasquez, J.C., Guerrero, J.M., Savaghebi, M., Eloy-Garcia, J., Teodorescu, R.: Modeling, analysis, and design of stationary-reference-frame droop-controlled parallel three-phase voltage source inverters. IEEE Trans. Ind. Electron. 60(4), 1271–1280 (2012)
31. Rouzbehi, K., Gavriluta, C., Candela, J.I., Luna, A., Rodriguez, P.: Comprehensive analogy between conventional AC grids and DC grids characteristics. In: *IECON 2013–39th Annual Conference of the IEEE Industrial Electronics Society*, Vienna, Austria, pp. 2004–2010 (2013)
32. Azizi, N., CheshmehBeigi, H.M., Rouzbehi, K.: Optimal placement of direct current power system stabiliser (DC-PSS) in multi-terminal HVDC grids. IET Gener. Transm. Distrib. 14(12), 2315–2322 (2020)
33. Saad, H., et al.: Modular multilevel converter models for electromagnetic transients. IEEE Trans. Power Delivery 29(3), 1481–1489 (2013)
34. Bergna, G., et al.: An energy-based controller for HVDC modular multilevel converter in decoupled double synchronous reference frame for voltage oscillation reduction. IEEE Trans. Ind. Electron. 60(6), 2360–2371 (2012)
35. Zhou, J.Z., Ding, H., Fan, S., Zhang, Y., Gole, A.M.: Impact of Short-Circuit Ratio and Phase-Locked-Loop Parameters on the Small-Signal Behavior of a VSC-HVDC Converter. IEEE Trans. Power Delivery 29(5), 2287–2296 (2014)
36. D'Arco, S., Suul, J.A., Beerten, J.: Configuration and model order selection of frequency-dependent π-models for representing dc-cables in small-signal eigenvalue analysis of HVDC transmission systems. IEEE J. Emerg. Sel. Top. Power Electron. 9(2), 2410–2426 (2021)
37. Kocar, I., Mahseredjian, J.: Accurate frequency dependent cable model for electromagnetic transients. IEEE Trans. Power Delivery 31(3), 1281–1288 (2015)
38. Rouzbehi, K., Miranian, A., Luna, A., Rodriguez, P.: DC voltage control and power sharing in multiterminal DC grids based on optimal DC power flow and voltage-droop strategy. IEEE J. Emerg. Sel. Top. Power Electron. 2(4), 1171–1180 (2014)

39. Safari, A., Shayanfar, H.A., Kazemi, A.: Robust PWMSC damping controller tuning on the augmented Lagrangian PSO algorithm. IEEE Trans. Power Syst. 28(4), 4665–4673 (2013)
40. Hassan, L.H., Moghavvemi, M., Almurib, H.A., Muttaqi, K., Ganapathy, V.G.: Optimization of power system stabilizers using participation factor and genetic algorithm. Int. J. Electr. Power Energy Syst. 55, 668–679 (2014)
41. Ebrahimzadeh, E., Blaabjerg, F., Wang, X., Bak, C.L.: Bus participation factor analysis for harmonic instability in power electronics based power systems. IEEE Trans. Power Electron. 33(12), 10341–10351 (2018)

How to cite this article: Azizi, N., Moradi CheshmehBeigi, H., Rouzbehi, K. Control strategy for direct voltage and frequency stability enhancement in HVAC/HVDC grids. IET Renew. Power Gener. 15, 3915–3926 (2021). https://doi.org/10.1049/rpg2.12307